The Morphology of Decorated Amyloid Fibers is Controlled by the Conformation and Position of the Displayed Protein

Christopher J. Forman,[†] Adrian A. Nickson,[†] Spencer J. Anthony-Cahill,[‡] Andrew J. Baldwin,[†] Gillian Kaggwa,[§] Urs Feber,[§] Khizar Sheikh,[§] Suzanne P. Jarvis,[§] and Paul D. Barker[†,*]

[†]Department of Chemistry, University of Cambridge, Lensfield Road, Cambridge, CB2 1EW, U.K., [‡]Department of Chemistry, Western Washington University, Bellingham, Washington 98225-9150, United States, and [§]UCD Conway Institute of Biomolecular and Biomedical Research, University College Dublin, Belfield, Dublin 4, Ireland

ABSTRACT Self-assembled structures capable of mediating electron transfer are an attractive scientific and technological goal. Therefore, systematic variants of SH3-Cytochrome b_{562} fusion proteins were designed to make amyloid fibers displaying heme-b_{562} electron transfer complexes. TEM and AFM data show that fiber morphology responds systematically to placement of b_{562} within the fusion proteins. UV—vis spectroscopy shows that, for the fusion proteins under test, only half the fiber-borne b_{562} binds heme with high affinity. Cofactor binding also improves the AFM imaging properties and changes the fiber morphology through changes in cytochrome conformation. Systematic observations and measurements of fiber geometry suggest that longitudinal registry of subfilaments within the fiber, mediated by the interaction and conformation of the displayed proteins and their interaction with surfaces, gives rise to the observed morphologies, including defects and kinks. Of most interest is the role of small molecule modulation of fiber structure and mechanical stability. A minimum complexity model is proposed to capture and explain the fiber morphology in the light of these results. Understanding the complex interplay between these factors will enable a fiber design that supports longitudinal electron transfer.

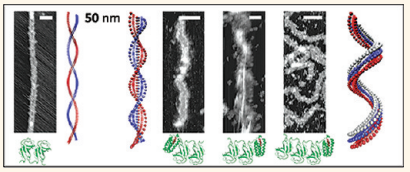

KEYWORDS: amyloid · molecular electronics · electron transfer · self-assembly · AFM

Increasingly, it is becoming apparent that most catalytic processes in cells occur in highly spatially controlled, organized assemblies. Examples are the remarkable α-ketoacid dehydrogenase enzymes,[1] metabolosomes,[2,3] and the respiratory[4] and photosynthetic[5] complexes. These highly evolved complexes, central to metabolism, result in sophisticated and optimal function within cells. Understanding how to use generic, self-assembling 3D scaffolds to display arbitrary enzymes in spatially defined superstructures might lead to viable general strategies for controlling the dynamic integration of material, information, and energy flows within artificial devices.

To this end, we have begun to use amyloid fibers to organize electron transferring heme proteins, cytochromes, into defined, self-assembling and flexible structures.[6] The spatial requirements for rapid interprotein electron transfer[7] place significant constraints upon any chain of cytochromes if such an assembly is to function as a flexible molecular wire. This strategy relies on understanding the relationship between the structure of the amyloid and the distribution of the cytochrome payload displayed upon it as well as the dynamics of the resulting assembly.

The hierarchical assembly of amyloid fibers involves the specific aggregation of monomeric β-sheet forming units into filaments, two or more of which can assemble into mature fibers. The β-strands within the filament cores are thought to be perpendicular to the fiber axis,[8] although some evidence suggests that in some cases this may not be true.[9] While significant progress has been made in the understanding of the extended β-strand structure of the core of representative amyloid protofilaments,[10] the higher order structures of these filaments are less well-defined. In particular, how is extra sequence, either unfolded or folded into well-defined domains, accommodated into the fiber superstructure?

The long-range morphologies of amyloid fibers, as they appear in low resolution transmission electron microscopy (TEM), are often described as elastic helical ribbons which can exist on a continuum between

* Address correspondence to pdb30@cam.ac.uk.

Received for review October 28, 2011 and accepted January 25, 2012.

Published online January 25, 2012
10.1021/nn204140a

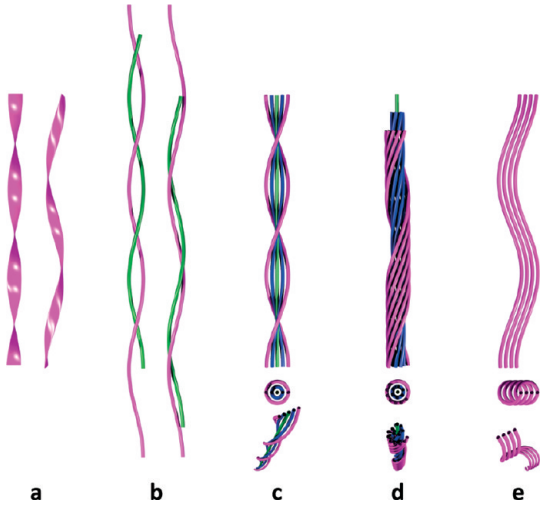

Figure 1. Combining filaments to make fibers. (a) In TEM amyloid fibers appear as continuous elastic ribbons on the transition between twisted and spiral ribbons. (b) Identical, coaxially aligned filaments may be displaced from each other longitudinally. In the schematic, the purple filament remains stationary while the green filament can be adjusted vertically to attain either twisted or spiral ribbon morphologies, while conserving the curvature of the filament. Maximum vertical displacement yields the twisted ribbon. (c) Combining filaments radially, as in the flat tape model,[17] requires modifying the torsion and curvature the further the filament is from the central axis. This suggests that protein monomers may adopt distinct conformations within each filament. (d) Conceivably, bundles of filaments can combine both longitudinally and radially to yield complex morphologies containing many protein conformations. (e) Relaxing the requirement for a common axis allows identical versions of the same filament to combine radially without modifying the curvature of the underlying helix; however, such structures are likely to be energetically unstable due to asymmetry in energetic interactions between neighboring filaments.

spiral and twisted extremes[11,12] (see Figure 1a). Such descriptions of elastic ribbons are not immediately compatible with the idea that fibers are bundles of filaments as suggested from the results of higher resolution amyloid studies using high resolution TEM (HRTEM), nuclear magnetic resonance (NMR), and X-ray diffraction (XRD).[8,13−16] The two descriptions are seen to be compatible by understanding the role of filaments in defining the overall morphology of the fibers.

Adjusting the longitudinal displacement of coaxially aligned filaments generates fiber morphologies on a continuum between spiral and twisted ribbons, as in Figure 1b. Such translations conserve the curvature of each filament. Conversely, flat tapes can be generated by adding coaxially aligned filaments to a bundle in a radial direction.[17] In this case, shown in Figure 1c, the outer filaments have the same central axis but modified curvature. Indeed, from the perspective of fiber stability and uniform nearest neighbors, both longitudinal and radial displacements could occur within the same fiber bundle, as shown in Figure 1d, if an appropriate hierarchical formation mechanism existed. Relaxing the requirement for a common axis with neighboring filaments also allows the filaments to combine radially without distortion as in Figure 1e. However, this scenario admits filaments into the bundle asymmetrically from an energetic point of view—the outer filaments have fewer nearest neighbors—which generates an energy budget to distort the filaments.[18]

Changing the curvature of a filament relative to its neighbors requires variation either in the conformation of the monomeric proteins, the elastic strain imposed on the monomers, the number of protein monomers per turn or a combination of all three. Such distortions clearly affect, and are affected by, the registration of the monomers between the filaments.[18] Insisting that the protein conformation remains conserved throughout a fiber therefore has consequences for filament alignment and, subsequently, the long-range morphology of the fiber.[19] The changes in morphology between the suite of protein fibers we examine here, suggest that the protein sequence *not* incorporated into the core amyloid structure strongly influences the final superstructure.

SH3 dimer ($SH3_2$) fibers have been found to form a range of morphologies, mostly twisted ribbons.[20] However, we have observed that fusing cytochrome b_{562}, an electron transfer protein, to the $(SH3)_2$ fiber-forming domain, such that every fiber-forming SH3 dimer unit has a cytochrome attached, results in fibers with spiral ribbon morphology.[6]

As heme is added to solutions of such fusion protein fibers, the fiber-borne cytochromes can change conformation by folding to form a heme complex that is essentially identical to monomeric holo-b_{562}[6] under the same conditions. Apparently, half of the fiber-borne cytochromes are available to bind heme with a high affinity for the cofactor similar to the WT protein.[6] Earlier NMR analysis suggested that the set of fiber-borne cytochrome domains that bind heme with high affinity are unfolded and flexible in the absence of heme allowing their detection by NMR despite being attached to such a large aggregate. The other 50% of the apocytochrome domains were not visible to NMR suggesting that this fraction of polypeptide has relaxation properties similar to that in the core of the fibers. This fraction also has a reduced affinity for heme, which leads to the hypothesis that the conformation of proteins in this fraction is restricted and cannot reach the native, heme binding structure without disrupting the fibers.

These observations prompted the current work in which we have studied five fusion proteins (see Figure 2 for nomenclature), each consisting of a different positional permutation of cytochrome b_{562} and the SH3 fiber-forming domain within a single polypeptide. We acquired substantial qualitative and quantitative morphological information about the fibers resulting from each of these variants, and their behavior under

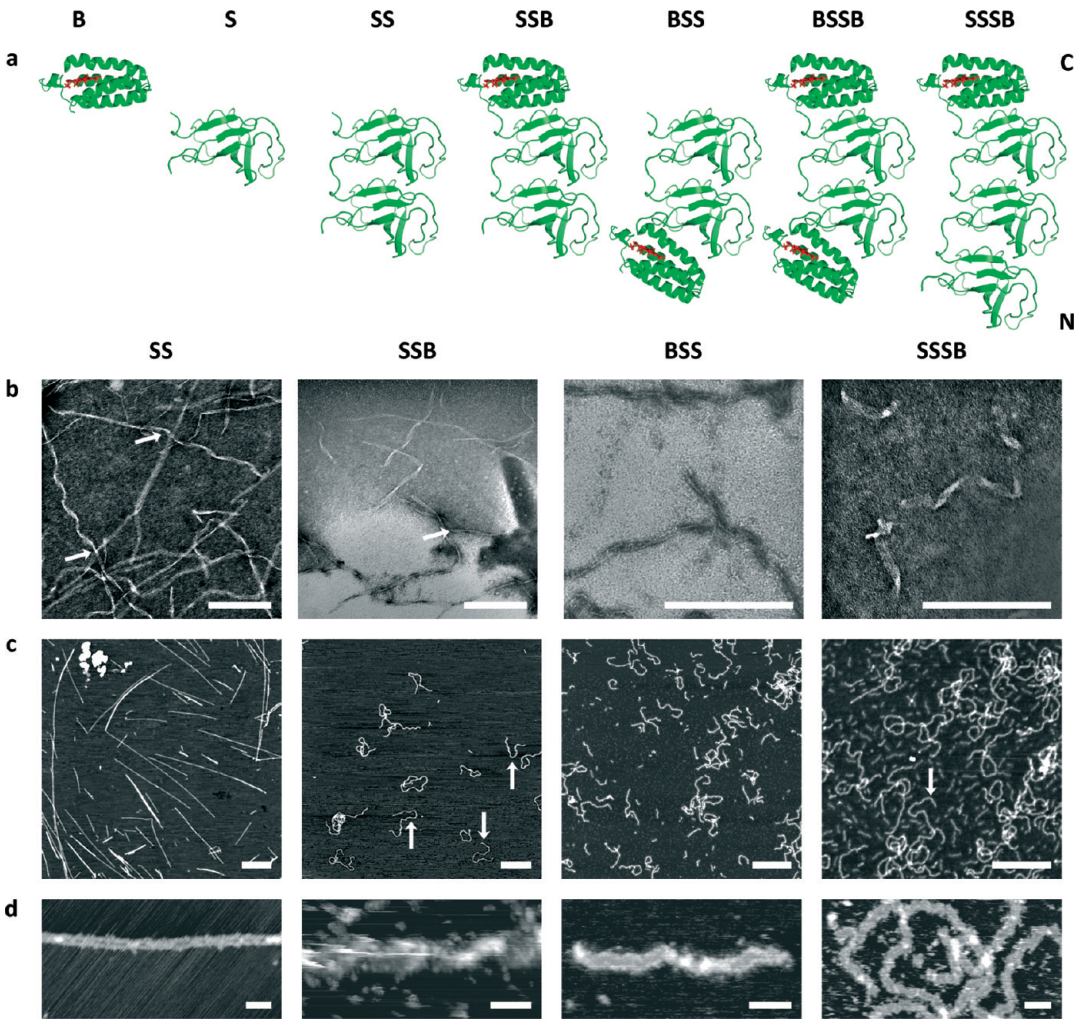

Figure 2. Fusion protein variants can form amyloid fibers. (Row a) The fusion variants are constructed from cytochrome b_{562}, denoted with "B", and the SH3 domain from phosphatidylinositol-3-kinase, denoted with "S". The cytochrome is a four helix bundle conformationally stabilized by complexation with heme. SH3 is predominantly β-sheet and, when in a misfolded form, readily forms fibers. The letters S and B are used to represent the order, from the N terminus to the C terminus, in which the domains appear in the given variants. The results of analyzing each fiber type are presented from the leftmost column to the rightmost, in the order SS, SSB, BSS, and SSSB, respectively. BSSB was not observed to form fibers. (Row b) Fibers negatively stained with uranyl acetate and observed by lrTEM with scale bars of 200 nm. The arrows in the SS and SSB images show morphology transition points. (Row c) lrAFM images of apo-fibers were acquired in air using a Dimension 3100 with tap 150 probes (tip radius < 10 nm). The arrows indicate a complex, irregular fiber shape that seems to be repeatedly adopted by the SSB fibers and once by the SSSB fibers. The scale bars are 500 nm. (Row d) hrAFM data of apo-fibers acquired under liquid (1 mM HCl) using a modified Asylum MFP instrument with low noise optics and nanosensor SSS-NCH probes (tip radius < 5 nm) scale bars, 50 nm.

heme binding, using TEM, low resolution AFM (lrAFM), and high resolution AFM (hrAFM) combined with UV−vis spectroscopy, has been studied. This has provided novel insights into the effect of an additional sequence, not incorporated into the amyloid core, and of heme binding upon fiber structure and mechanics.

RESULTS AND DISCUSSION

Characterization of Fibers Formed from the Fusion Protein Variants. A schematic of all five variants is presented in Figure 2, row a. Four of the variants generated fibers that were subsequently analyzed by TEM, lrAFM, and hrAFM, and typical results of that analysis, presented for the case with no heme (apo-fibers), are presented in Figure 2, rows b—d. It is striking that, under the same conditions in which all the other fibers formed successfully, BSSB was not observed to form fibers.

After deposition on a surface, the fiber variants are observed to possess complex and variable morphologies which depend on many factors including fiber entanglement, the details of the adsorption onto the surface, and the stochastic fluctuations of the fibers prior to the adsorption. All of these factors distort any quantitative measurements of the distribution of fiber morphologies and are difficult to control.

Low Resolution TEM Results. The lrTEM data in Figure 2, row b, also show that the SS fibers (left-hand panel) are observed as both twisted and spiral ribbons.

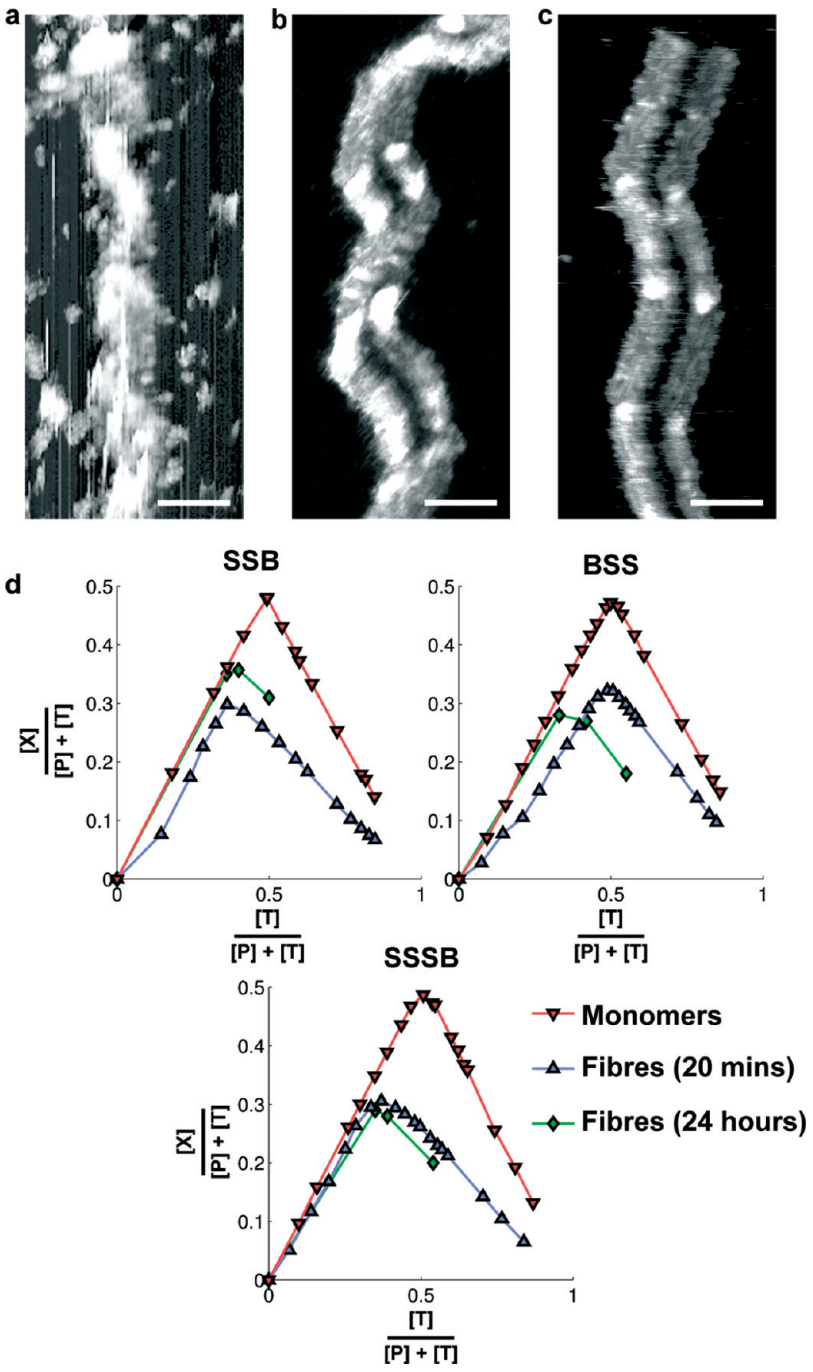

Figure 3. (a–c) High resolution AFM of SSB fibers imaged under 1 mM HCl (pH 3) after equilibrating in solutions with 0:1 (0%), 1:2 (50%), and 1:1 (100%) ratios of heme/protein, respectively. As heme binds the quality of the AFM images improve to reveal substructure. The scale bars are 50 nm. (d) Heme is added to solutions of SSB, BSS, or SSSB fusion proteins and monitored by UV–vis spectroscopy. [T] is the overall concentration of heme (bound and free), [P] is the concentration of protein, and [X] is the concentration of bound heme. The *x*-axis is the total mole fraction of heme, and the *y*-axis is the mole fraction of bound heme. In one experiment aliquots of heme are added every 20 min to solutions of either monomers (red downward pointing triangles) or fibers (blue upward pointing triangles). In a second experiment heme is added once to different vials of protein in varying proportions, and each is observed 24 h later (green diamonds). The *y*-ordinate of the maxima (*yMax*) indicates the stoichiometric ratio of heme and protein while the *x*-ordinate (*xMax*) indicates the excess heme required to achieve this. In most cases the *xMax* = *yMax* indicating that no heme excess is needed. These data indicate that all the fibers bind half as many heme molecules as there are cytochromes available (*yMax* = 0.33). In the 20 min regime, BSS requires more overloading than any other species.

The arrows in this panel highlight transition points between twisted and spiral ribbons within individual fibers. These transitions occur at contact points with other fibers in the surrounding network. Such strain-induced morphological transitions have been reported for helical lipid springs.[21]

By contrast, the remaining fiber types formed only spiral ribbons. There may be an internal morphology transition, indicated by the arrow in the second panel for SSB fibers, again occurring at the point of contact between two fibers. The third panel shows that BSS is very similar in overall appearance to SSB and the final panel indicates that the principal axis of an isolated apo-SSSB spiral ribbon fiber fluctuates strongly. In some cases, spherical aggregates were also observed, which may be significant.[22]

Low Resolution AFM Results. Figure 2, row c, confirms that the fibers are formed and are amenable to analysis by AFM in air on mica. The most obvious result is the induction of the more complex morphology in SSB, BSS, and SSSB fibers which has been brought about by the introduction of the cytochrome. However, given that spiral ribbons are present in the TEM data for SS, it may be that adsorption of the SS fibers on mica also plays a role in their relative straightness. This suggests immediately that the interplay between interfilament forces and the adsorption forces between the fiber and substrate play a role in the apparent morphology of the fiber.

The apparent morphologies of the remaining three species are in better agreement between AFM and TEM. The wide dispersion of fibers in some of the AFM images eliminates entanglement as the root cause of fiber kinks.

Despite the increased complexity of the fiber morphology due to the cytochrome, and the stochastic fluctuations of the morphology induced by Brownian motion in solution followed by the disruptive adsorption process, there exist recurrent complex shapes. These are indicated by the arrows in row c, that differ only in rotation and reflection from each other and this is evidence of systematic morphological behavior on adsorption. It seems unlikely that three such similar shapes would form randomly in such a small area, when the variation in the other shapes is much higher. Another example of such conservation of morphology is presented in Supporting Figure 1.

High Resolution AFM Results. A great deal of insight arises from hrAFM, shown in Figure 2, row d. Connecting material between the two SS filaments can be seen as well as the crossover points of the filaments.[17] Moving from left to right, the surface texture changes between the different fiber types which is consistent with the presence of flexible, unfolded domains observed by NMR on the cytochrome containing fibers.[23]

This high resolution information enables enumeration of the filaments within each fiber type both from the profiles of the fibers and from accounting for the pattern of crossover points within each fiber system.[17] However, if multiple filaments cross at the same point then such degeneracy can lead to ambiguity in the estimate of the number of filaments.

Close inspection of the high resolution data shows that the BSS and SSSB fibers can bend in the same direction on successive segments, whereas the SSB fiber tends to alternate. The SSB primary axis, over longer distances, therefore tends to be straighter.

The skirts surrounding the fibers in the AFM images suggest higher adsorption forces on mica than on the carbon film used in TEM. It is presumed that flexible surface moieties on the underside of the fiber wet the mica surface and spread out. This is particularly clear in Supporting Information, Figure 1.

After adsorption to the surface, additional strain induced at the crossover points may account for the high background count of SSSB fragments in Figure 2, row b, which are roughly the same length as individual segments of fiber. This fragmentation effect is only observed by AFM, and not TEM, again indicating a higher adsorption energy on mica than on carbon film which is consistent with the observation of surface wetting on mica. Similar clusters of fragments are shown for the other fiber types in Supporting Information, Figure 2. The fragments appear in groups that are not colinear and in which fragments never touch each other. This suggests a complex fragmentation process on adsorption in which the fragments may remain connected by loose material. In some cases there is a layer of material, about the same height as the skirts on individual fibers, surrounding the fragments.

Short isolated segments of fiber are subsequently referred to as "fragments" as opposed to repeating units within a full fiber, which are referred to as "cycles".

In certain cases, due to the high resolution of some AFM data, convolution free measurements of the *lateral* fiber dimensions can be acquired. For example the width of the fiber can be measured as the distance between the maximum points of adjacent filaments.

Heme Binding Results. Comparison of each fiber type in the presence of different concentrations of heme reveals that the fiber surface becomes better resolved by hrAFM as the heme-cytochrome complexes form. Figure 3 a—c, shows hrAFM images of SSB fibers taken from equilibrium solutions containing 0%, 50%, and 100% heme/cytochrome ratios. At high concentrations of heme the fiber substructure becomes clearly visible (Figure 3c).

Earlier NMR experiments on apo-fibers in solution detected flexible regions which were shown to consist of cytochrome b_{562} and part of the SH3 domain within the fiber. These became undetectable following heme binding.[24]This suggested that the cytochrome becomes more ordered on the surface of the fiber once it folds and binds heme, and its movements in solution are then correlated with those of the fiber as a whole. It is therefore likely that the surface features observed in Figure 3a—c contain individual cytochromes.

UV−vis spectroscopy detects ligation differences between heme in the free and complexed state which

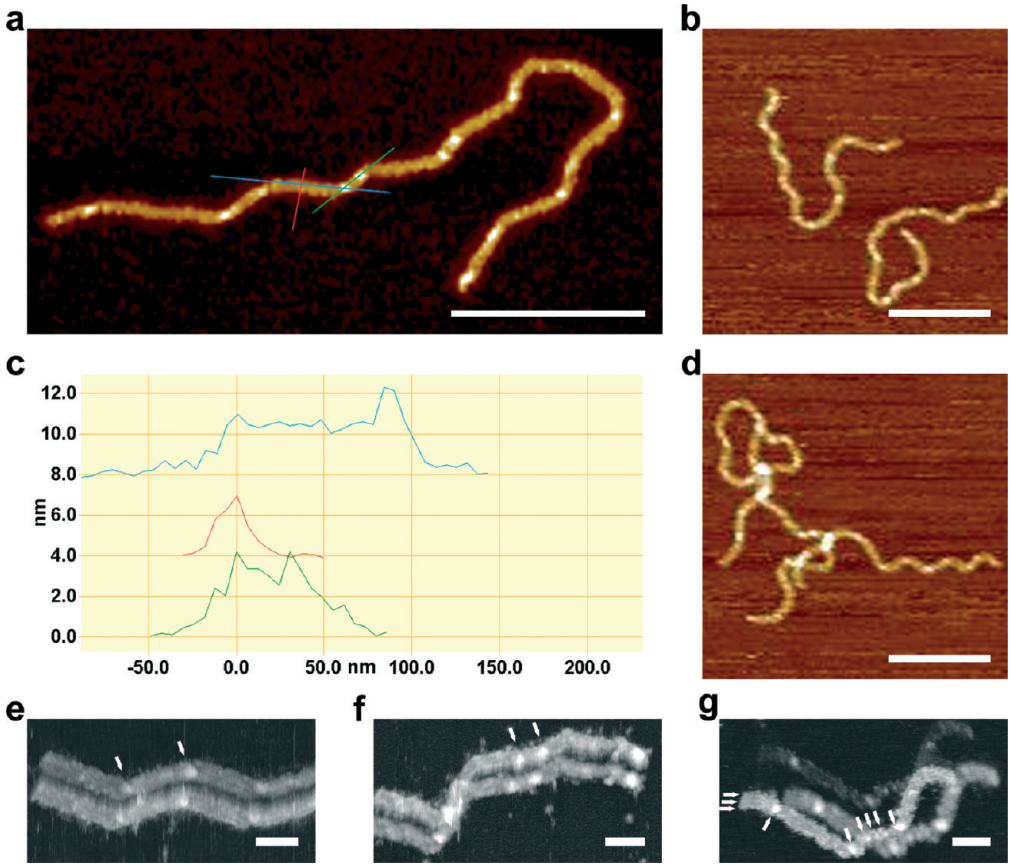

Figure 4. (a) The existence of peaks along the backbone of this apo-SSB fiber is indicative of fiber crossover points which may be degenerate (unresolved multiple filaments crossing at the same point). (b,d) The distribution of peaks along these SSB apo-fibers changes when the fiber morphology changes but not the overall number of peaks per cycle; 250 nm scale bar. (c) These profiles demonstrate that the peaks are the same height as the main fiber. (e–g) High resolution AFM data of holo-fibers. The arrows indicate the crossover points of the filaments.

allows monitoring of the effect of the fibers on heme partitioning. Knowledge of the extinction coefficients of bound and free heme at pH 3 must be acquired before deconvolution of the spectra is possible (see Supporting Information, Figures 3 and 4).

The graphs in Figure 3d show the mole fraction of heme that has formed complexes with cytochrome b_{562} in a variety of circumstances. The *y*-axis shows the mole fraction of bound heme and the *x*-axis indicates the total mole fraction of heme that has been added to the solution.

In one set of experiments, small amounts of heme are added every twenty minutes to solutions of fusion protein which is present either in monomeric form (red, downward pointing triangles) or in fiber-form (blue, upward pointing triangles). The heme distributes between free and protein bound states according to the apparent equilibrium heme binding constants and stoichiometries for these conditions. The maximum of the curve indicates that the stoichiometric ratio of bound heme/protein has been reached for that form of protein.

For the monomers (red lines) the maxima occurs at (0.5, 0.5) indicating that, at maximum, half of the objects in solution are bound heme (the other half are proteins) so the monomers bind heme in 1:1 stoichiometry.

In the case of the fibers (blue lines) the maxima occur for SSB at (0.36, 0.29) and SSSB at (0.31, 0.37) which is within experimental error of the maxima (0.33, 0.33) for a binding stoichiometry of 1:2 heme to fiber-borne b_{562}, in agreement with previous results for SSB.[24]

The maxima for BSS fibers is at (0.50, 0.32). The *y*-maximum of 0.32 indicates that the total number of binding sites available is half the number of proteins, as is the case for the other fibers, but the *x*-position of 0.5 indicates that an excess of heme must be added before these sites can be occupied.

In a second set of experiments (plotted as green diamonds) SSB, BSS, and SSSB fibers were each prepared at 50%, 75%, and 100% heme to cytochrome ratios, and the heme binding in all nine cases was observed after 24 h. The three data points characterize the maximum, which occurs for all three fiber species within experimental error of (0.33,0.33). Taking both experiments into account it is concluded that all the fibers types saturate high affinity binding sites at 50%

binding and the kinetics of heme binding to the BSS fibers are much slower than in SSB or SSSB fibers.

Analysis of Fiber Morphology. The consequences of modifying the fusion protein or heme binding state on the morphology of the fiber can only be determined if the morphology of the fiber can be quantified reliably. The obvious complexity of the fibers and the experimental limitations, such as adsorption and stochastic fluctuation, make this extremely challenging.

The AFM and TEM data can be analyzed statistically by measuring each well-defined cycle of a fiber. The key parameters are the length, L, and diameter or radius, $D = 2R$, of the cycle as well as the width of the fiber, W. However, not all the fibers are well behaved along their entire length. Therefore, to assist with this analysis, all the protein observed by TEM and AFM can be *objectively* grouped into one of five different classes:

1. short fragments, typically about the same length as the straight segments in a fully formed fiber, as well as any monomeric or oligomeric species
2. isolated fibers with clear periodic cycles
3. isolated fibers that were distorted or stretched
4. fibers tangled or in contact with other fibers
5. amorphous or spherical aggregates

The first class of fibers, individual fragments, can be characterized easily by measuring the length of their longest axis. Class two fibers are measurable using the techniques described in the Materials and Methods section and which are illustrated in Supporting Information, Figures 5 and 6. Class two and class three fibers can also be characterized by measuring the internal angle between the segments, often straightened by adsorption. This technique allows class two and class three fibers to be grouped into a single class.

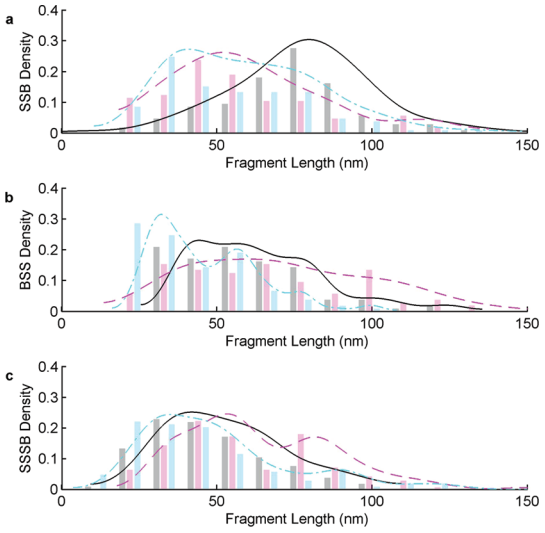

Figure 5. Fragment Analysis. The distribution of fragment lengths for (a) SSB, (b) BSS, and (c) SSSB. All the fibers were observed to fragment into small pieces. Every class one object within a 1 μm square area of an AFM image was measured along its longest axis. This was repeated, moving systematically through the image, until at least 100 objects had been measured, ensuring that all the objects in the final square had been measured. The density of the distribution was estimated using one-dimensional kernel density estimation,[25] which contains the same information as a histogram which is presented for completeness. The effects of adding heme are represented by the magenta columns and dashed line (50%) and the cyan columns and dashed−dot line (100%). This measurement of the fragment length suffers from the effects of tip convolution.

TABLE 1. Fragment Distribution Modes[a]

species		modal fragment length (nm)					
SSB	0%	45?		80	100?		
	50%	35	52	80		118	
	100%	41		74			
BSS	0%	44	56	75	100	122	
	50%	42	62		100		
	100%	32	57	77	100		
SSSB	0%	42	60	85			
	50%	41	54	81		113	150
	100%	35	49	89		117	172
average		40	54	80	100	117	161
Δ average		14	16	20	17		

[a] The fibers break up into fragments and the distribution of the fragment lengths has a multi-modal nature. Although the occupancy of each mode varies among the fiber types and conditions, the position of these modes is consistent across the fiber types (and subject to tip convolution). The question mark indicates that the occupancy of a mode is too small to display a distinct peak, but there is definitely an extremum in the derivatives of the distribution at this point.

TABLE 2. Number of Fragments Per Fiber[a]

type	0% heme	50% heme	100% heme
SSB	1.6	4.0	10.0
BSS	1.7	1.7	7.1
SSSB	1.1	22.2	3.3

[a] Shows the number of fragments per fiber as computed by counting all the fibers and fragments within two images for each species and heme condition. The number of fragments per fiber increases under the addition of heme and decreases in response to the changes to the fusion protein.

Fibers from the fourth class are well-defined and were completely ignored in the analysis. Objects in the fifth class are large aggregates which are rare and can easily be avoided during the data acquisition process. These are not considered further here.

Any bias arising from the observer's choice of objects to measure was eliminated by measuring every object in the field of view that could be measured. The surface adsorption procedure was identical for all the fibers, so any bias observed in the data is a byproduct of the nature of the samples.

Fibers were analyzed under three different ratios of heme to protein mixtures; 0%, 50%, and 100%. It is important to note that under the conditions of analysis,

at the 50% ratio all the heme is essentially bound to protein. However, at the 100% ratio, half of the heme is bound but the other half of the cytochrome sites may not all be occupied.

Quantitative Analysis of Fiber Morphology. In the subsequent analysis, first the number of filaments in each fiber are enumerated and then each class of object is examined in turn.

Number of Filaments. The crossover points, cross sectional profiles and complex bending behavior can be used to measure the number of filaments in each fiber type, as illustrated in Figure 4.

For SSB fibers, the two crossover points per cycle in both Figure 4a and e suggest there are two filaments. This is supported in Figure 4b and d despite either a morphological change or a distortion due to adsorption.

The BSS fiber in Figure 4 also has two crossing points, which suggests a two filament fiber. However, the bending behavior is somewhat erratic, with highly variable segment lengths. Such variation in segment lengths is consistent with the presence of more filaments, or a more complicated interaction between the filaments.

The SSSB fiber in Figure 4g possesses three filaments, indicated by the arrows at the end of the fiber. With no degeneracy three filaments should generate six crossing points per cycle, and six candidate peaks are found within the same cycle as indicated by the arrows.

Earlier high resolution AFM data (Figure 2, row c,) indicates unambiguously that there are two filaments in the SS fibers, which is consistent with published structure of fibers made from pure SH3.[10]

Thus SSB possesses two filaments; SSSB, three; and SS, two. The situation for BSS is ambiguous since the crossover-points suggest two filaments but the erratic behavior, which is more consistent with the SSSB fibers, suggests three filaments.

Analysis of the Class 1 Fragments. The fragments were present in all fiber systems and heme conditions and their length and heights are typical of the length and height of one segment of fiber. Figure 5 panels a, b, and c present the multimodal distribution of the fragment lengths acquired from measuring over 100 fragments per species. It is striking that there are several modes in each distribution and that the modal values are roughly conserved across all the species, as summarized in Table 1.

The mean modal values are computed and displayed in the penultimate row of Table 1. The relationship between them is clearly linear and the fragments are probably formed by units around 15−20 nm in length. The first mode is two such units, the second mode is three, and so on. During measurement it was a regular occurrence to observe low peaks that were separated by approximately 15−25 nm.

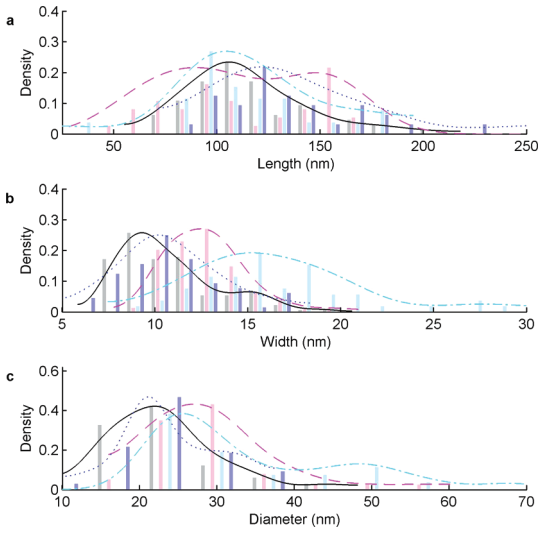

Figure 6. Experimental trends from TEM. (a) Length, (b) width, and (c) diameter of SSB (black/solid), BSS (magenta/dashed), SSSB (cyan/dashed-dot), and SS (blue/dotted) apofusion variants measured from TEM images. The histograms are presented alongside the KDE of the distribution function from which the sample was taken. The average values and sizes of the data sets are presented in Table 3.

The observation of more than four peaks was rare. The upper two modes (∼117 and ∼161) are not very important because there are few fragments within them.

As the amount of heme increases, so the relative number of mode one and two fragments increases. It is likely that more protein monomers or dimers are breaking away from the fibers the longer fibers are exposed to an excess of heme. The distributions of SSB, BSS, and SSSB fragment lengths become remarkably similar in the presence of heme.

The number ratio of fragments to fibers changes as heme is added which is summarized in Table 2. It is clear that as heme is added the number of fragments increases, which is consistent with the emergence of shorter fragments. This occurs for all the species. Considering the 100% column, it seems that SSB produces more fragments than BSS, which, in turn, produces more fragments then SSSB. One of the scanned regions of a sample of SSSB 50% heme fibers contained a layer of fragments that completely covered the scanned area and the resulting number ratio is therefore atypically higher than the other values in the table. This value is included to highlight the fact that such extreme coverage of fragments was never observed for apo-fibers, although it was observed in a number of cases for holo-fibers as shown in the Supporting Information Figure 2. Altogether, the data in Table 2 is consistent with the interpretation that adding heme increases the level of fragmentation regardless of species.

Analysis of Class 2 Fibers by TEM and AFMTEM Analysis. A collection of TEM images was statistically

TABLE 3. Summary of Class 2 Apo-fiber Parameters[a]

		L (nm)			*D* = 2*R* (nm)			*L*/*D*			*W* (nm)	
		TEM	lrAFM		TEM	lrAFM		TEM	lrAFM		TEM	hrAFM
type	*N* (M)	mean	mean	mode	mean	mean	mode	mean	mean	mode	mean	s.m.
SS	32 (7)	142			23.8			5.9			11.1	10.7
SSB	64(18)	114			23.1			4.9			9.8	13.5
	14(9)		108			21.0			5.1			
	14(9)			94			17.2			5.4		
BSS	37(19)	112			29.1			3.8			12.9	11.3
	40(16)		94			20.8			4.5			
	40(16)			104			21.4			4.9		
SSSB	26 (6)	114			39.3			2.9			16.5	15.0
	47(19)		81			20.8			3.9			
	47(19)			67			13.0			5.2		

[a] The column labelled N(M) indicates that N cycles were measured from M distinct lone fibers. The next two columns compare the *L* and *D* values arising from the TEM and AFM data presented in Figure 6 and Figure 7. In the final column the letters s.m. indicate a single measurement of *W* from high resolution AFM images.

analyzed and the resulting distributions of *L*, *D,* and *W* for the class two fibers are shown in Figure 6 only for the apo-fusion variants.

The distributions comprise a peak which is approximately normal and a heavy tail which indicates stochastic fluctuations. The means of these distributions are summarized in Table 3 alongside similar results from low resolution AFM data. The distributions for SSB are well formed with well-defined variance. The distributions for BSS and SSSB are broader with less well-defined peaks.

The largest change in *L* arises from adding the cytochrome. There appears to be no significant change in *L* based on where the cytochrome is placed. $D = 2R$ is the same for SSB and SS, but BSS and SSSB seem to possess wider cycles. The fiber width *W* increases in the order SSB, SS, BSS, SSSB and this sequence is consistent with the numbers of filaments reported above, where, again, there is some ambiguity concerning BSS.

Low Resolution AFM Analysis. Samples of SSB, BSS, and SSSB fibers were taken from solutions of 0%, 50%, and 100% heme/protein ratios and imaged by AFM. Cycle lengths and diameters of class two fibers in all nine experimental cases were analyzed. *W* was not analyzed because the effects of tip-convolution cannot be corrected in every case. The probability density function for each *L-vs-D* distribution was estimated using the two-dimensional kernel density estimation (KDE) implemented in Matlab[25] and presented as bivariate distributions in Figure 7a,c,e. The information presented using this nonparametric technique is equivalent to a histogram.

As in the TEM analysis, the data show Gaussian peaks with heavy tails. The distributions are very broad with lengths between 40 and 150 nm, and diameters between 5 and 50 nm. The mean values of the distributions of the *apo*-fibers, represented by the positions of the cross hairs, are presented alongside values from TEM as shown in Table 3. The variation among these mean values is small, but the *shape* of distributions contain more information. In all cases there is a weak correlation between the distributions for *L* and *D*, suggesting that the angle between the segments is sufficient to characterize the fibers.

In Figure 7 panels a, c, and e the superimposed contours depict the effect of heme which can also be assessed by the changes in the cross hair locations under heme binding. The length of the arms of each cross are the standard error of the underlying distribution, which is an estimate of the standard deviation in the position of the sample mean. This indicates the interval in which we would expect to find, with 68% confidence, the mean for a completely different sample of fibers. Doubling the length of the arms would give the 95.4% confidence interval.

The data support the argument that heme could affect the morphology of the fibers but that the effect is very small compared to the variation within the distributions making it difficult to measure the proposed effect.

The $L-D$ distribution for apo-fibers (Figure 7e) is bimodal indicating two predominant sizes for an SSSB fiber cycle. For each of these modes, the ratio of L/D is the same. The 50% sample does not appear to be bimodal and is centered near one of the modes. The 100% sample is also bimodal. This bimodality is supported by the TEM data in Figure 6.

The comparison of the *L* and *D* values in Table 3 reveals the changes in morphology that arise from modifications to the position of the cytochrome. However, these results are hard to interpret because the trend across the fusion proteins seems to depend on the analysis method and statistical quantity considered, for example, whether the data was acquired by AFM or TEM and whether the mean or modal average of a particular parameter is considered.

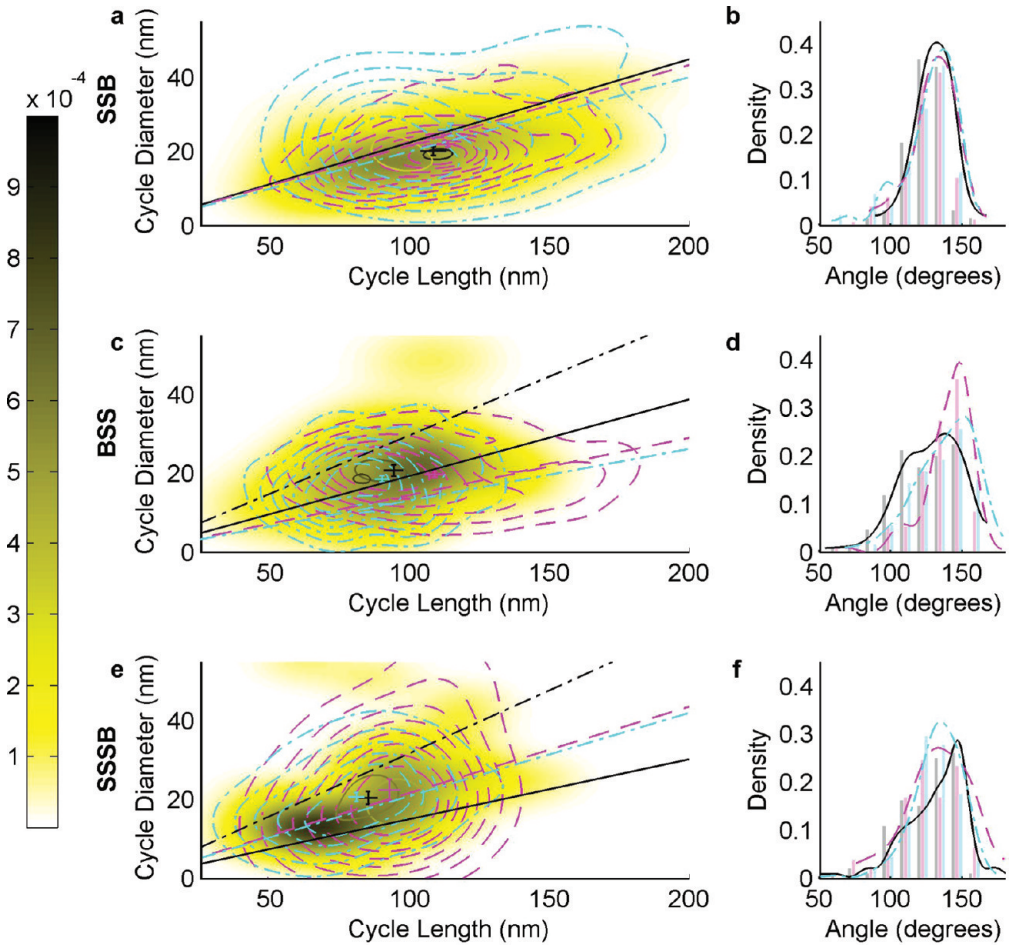

Figure 7. Low Resolution AFM analysis. (a,c,e) The distribution density of the cycle lengths and diameters of the class-two fibers are jointly estimated from the sample sets and presented as a surface viewed from above. The density at a particular set of parameters, indicated by the color bar, estimates the proportion of the population which have those parameters, as in a histogram. The effect of adding heme is shown by the contours. The dashed magenta contours represent the 50% case, and the cyan dashed-dot contours represent the 100% case. The highest contour is colored according to the color bar. The sample mean of each data set is indicated by a cross, the length of whose arms are the standard error of the underlying sample. The black cross represents the 0% case, magenta is the 50% case, and cyan is the 100% case. (b,d,f) The distribution of the inner angle between segments is presented for the 0% (solid, black line), 50% (dashed, magenta line) and 100% (dash-dot cyan line) heme loading cases for the combined class two and three SSB, BSS, and SSSB fibers. The primary modal values of the angular distributions are superimposed on the plots a, c, and e as lines corresponding to a particular ratio of *L*/*D* with colors and line styles matching the angular distributions. The secondary mode of the angular distributions for BSS and SSSB are apo-fibers which are plotted as black dashed−dot lines.

Comparing the mean values from TEM and AFM shows two distinct trends. In TEM the mean *L* value is roughly conserved across the species, whereas *D* varies systematically. In contrast, the mean values from the AFM data show that *D* is roughly conserved, whereas *L* varies systematically. This may indicate that between them *D* and *L* only possess one degree of freedom, which is consistent with helical symmetry. The results here suggest that such a degeneracy could manifest differently in TEM or AFM, presumably due to differences in the adsorption process, for example surface wetting or molecular combing.

The *modal* averages of the AFM data are not as sensitive to the effects of the fluctuations as the mean averages and so are more reliable. Both the *L* and *D* modal averages increase systematically in the order SSSB, SSB, and then BSS and, furthermore, the ratio *L*/*D* is very similar regardless of species, indicating similarity in the core helicity of each fiber. Therefore the data indicate that each species is seen to have a preferred cycle size, while both the proportions of those cycles and the range of their fluctuations are conserved across the species.

The difference between the mean and the mode is indicative of the level of fluctuation displayed by the fiber and SSSB can be seen to fluctuate the most followed by SSB and then BSS.

AFM measurements of fiber width usually suffer from tip convolution but the resolution of multiple filaments circumvents this limitation allowing unprecedented agreement between TEM and a single measurement of fiber width from high resolution AFM data.

TABLE 4. Mean Angles between Segments[a]

type	0% heme (deg)	50% heme (deg)	100% heme (deg)
SSB	132	133	136
BSS	138	148	151
SSSB	146	133	134

[a] All values are in units of degrees. The error in each measurement is estimated at 2.3°. The number of angles measured in each case varies between 60 and 142 which were taken from every isolated fiber that was available in each image set. For BSS and SSSB the angle changes dramatically on the addition of heme which proves that the morphology of the fibers can be directly influenced by small molecule control *via* the conformation of displayed proteins.

Analysis of Class 2 and Class 3 Fibres Using AFM. The measurement of the angles between adsorption straightened segments allows characterization of the more complex class 3 fibers. This set of measurements can be joined to the set of angles measured for the class 2 fibers, which expands the size of the data set and yields distributions with very well-defined peaks and much smaller variation as presented in Figure 7b,d, f. The largest angular error arises from the subjective placement of the angle measuring tool which was estimated at ±2.3° by assessing the variability of repeated measurements of a set of five angles using the method described in Supporting Information, Figure 5.

In general this means that any two consecutive segments can be completely characterized by their internal angle and size. In the case of BSS and SSSB (Figure 7d,f) the angular distributions are bimodal implying the existence of two classes of angles between distinct types of segments in the fibers. Inspection of the high resolution fibers in Figure 2d, Figure 3a—c and Supporting Information, Figure 4e—g, shows a variety of angles and angle types between distinct types of segments.

The internal angles (~140°) correspond to the ratio of *L* and *D* (~5.0), which can be plotted as a straight line on the *L vs D* distribution. Assuming that each cycle collapses symmetrically as a perfect isoceles triangle allows the superposition of the primary and secondary modal values of the angular distributions in Figure 7a,c,e. This explicitly reveals the consistency between the angular and *LD* data.

The variation in size of a cycle as one moves along this line can be accessed by torsional distortion of the fiber which conserves the pitch angle of the helix (*i.e.*, both *L* and *D* change in proportion with each other), while the variation perpendicular to this line, corresponds to bending the fiber.

The fact that the secondary mode (black dashed lines, Figure 7) correspond to distinct variations in the underlying shape of the *L vs D* distribution serves to emphasize consistency between the *L* and *D* distributions and the angular distributions.

The bimodal nature of the SSSB *L* and *D* distribution results in two classes of size for the SSSB fibers. The larger size is around 90−100 nm in length and 20 nm in diameter, which is quite close to the modal values of SSB and BSS and preserves the ratio *L*/*D*. The smaller (more populated) SSSB mode was included in Table 3. In addition, the bimodal nature of the angular distribution results in two angular classes. The two angular classes do not correspond to the two size classes.

Table 4 summarizes the primary modal angles for all heme states and fiber types. The SSSB fibers have a larger internal angle than both the SSB or BSS fibers, and one would expect them to be straighter than SSB or BSS over a long-range. However, as observed previously the SSSB fibers bend in the same sense on successive segments, rather than alternately as in the case of the SSB fibers. Therefore SSSB fibers are more erratic that the straighter SSB fibers. This is very clear in Figure 4g.

Complex bending behavior may be further evidence of three filaments in the SSSB fibers. Close inspection of the BSS also exhibits complex bending behavior strongly supporting the arguments that BSS contains three filaments.

On binding heme, the primary mode angles of the BSS and SSSB fibers change by 10° and 13°, respectively, but, strikingly, in the opposite sense, the BSS fibers straighten whereas the SSSB fibers become more acute, and more like the SSB fibers in which the primary mode angle does not change significantly under heme binding. The transition from apo-fibers to 50% heme fibers accounts for the bulk of the angular change. The lesser angular modes of the BSS and SSSB fibers do not move on heme binding, although the occupancy of this mode reduces for BSS but not SSSB.

There is little doubt from this information that the heme significantly affects the segment angles and, all else being equal, the quantitative differences between the SSB, BSS, and SSSB angular distributions must be explained either by changes in position of the cytochrome, the addition of the extra SH3 domain in SSSB or the conformation of the cytochromes. This is clear evidence that the long-range morphology of the fibers can be controlled by the folding and subsequent molecular packing of noncore material.

Discussion. We believe that the classes of fibers presented in the analysis are variously distorted members of the same population of fibers which, in solution, would be stochastically fluctuating spiral or twisted ribbon fibers. The process of adsorption acts to pull the fiber flat against the surface which could be viewed as a deliberate perturbation, thereby accessing experimental regimes that are actually overlooked in bulk techniques. Furthermore, since the intended use of these materials will most likely require them to be adsorbed on solid supports the analysis presented here is more informative than that derived from solution phase

analysis. This detailed multidimensional analysis generates a number of arguments to support the following general points.

The Core Structure May Be Independent of Cytochrome Position. The core structures of all the fibers may be the same. This is supported by the fact the modal values of the fragment sizes (Figure 5) are the same regardless of the species and that as the fibers fall apart the fragment distributions tend toward the same limit. The modal values of the cycle sizes and internal angles in each fiber system are very similar indicating a similar mechanical resistance to adsorption. Although there are clear changes to the angles on heme binding, the overall angle does not change a great deal, indicating that the adsorption behavior is dominated by the core of the fiber.

As Heme Is Added the Fibers Become More Unstable. Whether the fragments form on adsorption or in solution, fragmentation is more likely to occur when the fiber is packed with heme. This suggests that the cytochromes on the fibers pack together more densely under the influence of heme and that the resulting fibers become more unstable. This supports the hypothesis that the 50% heme binding phenomena arises from overcrowding on the surface of the fiber. Heme binding in the high affinity sites folds the cytochrome into its native structure and leads to close packing of cytochrome units (as evidenced by the improved imaging properties) which can be accommodated without energetic penalty on the filament surfaces. Further heme binding into the remaining sites leads to an energetic penalty due to increased axial stress which is relieved by significant fiber disruption, yielding larger numbers of monomeric and dimeric fragments (Figure 5). We predict that complete occupation of heme sites cannot be achieved over a full helical turn and this explains why fibers cannot be formed starting from the holoprotein.

The Cytochromes Mediate Much of the Contact between Filaments in the Fiber. Although the basic mechanics of the fiber is dominated by the elasticity of the core, the ability to resist adsorption is strongly modified by the position and conformation of the cytochrome which has been shown by documenting the way in which the filaments within the fibers unravel and flatten against the substrate. The surface texture, crossing points, size of internal angle, and cycle size distributions are all consistent with a model in which the energy of adsorption and the elasticity of the core are precisely balanced in equilibrium on the surface. This means that only small changes in the cytochrome conformation are needed to affect this balance. This conclusion also leads to the hypothesis that defects arising from the mis-registration of the cytochromes lead to kinks in the long-range backbone of the fiber. There is no evidence as to whether or not these kinks exist in solution or only when fibers are adsorbed onto surfaces.

The Position of the Cytochrome Determines the Change in Angle after Binding Heme. The idea that the central fiber core is highly conserved across the species is supported both by the fragment analysis and the conservation of helicity (*L*/*D* ratio) across the cytochrome bearing fibers. If the cores are the same then the cytochrome in the BSS fibers is likely to occupy the same position as the additional S in the SSSB fibers. In this case adding heme to the BSS fibers would cause stress in a different place within the fiber structure; presumably on the opposite side of the filament to the cytochrome in the SSB and SSSB fibers. This could account for the opposite effects of heme binding in BSS and SSSB fibers. However, since cytochrome b_{562} and the SH3 domains are roughly equal in size (106 and 86 residues, respectively), they could have a comparable effect on fiber morphology when considering size exclusion effects alone. To provide insight in this regard a single control sample of SSS fibers was analyzed by TEM which showed the SSS fibers to be straight, twisted ribbon morphologies, much like the SS, indicating that the introduction of the cytochrome is responsible for most of the morphological change and the details of how it affects the fiber depend on precisely where it is in the structure. In the SSSB fibers, if all three SH3 domains are involved in the core then the cytochrome positions are likely to be spaced further apart relative to the underlying helical structure, giving the space for three filaments to entwine successfully. In the SSB fibers, the position of the cytochrome is such that heme binding has no observable effect on morphology.

General Physical Considerations. Both the mechanical response of the fiber and the strength of the interaction with its environment play a role in determining the overall behavior of the fiber and the displayed material plays a role in both of these factors. The detailed response of the fiber to random forces in solution depends on the mechanical properties of the fiber, such as the Young modulus, torsional modulus, and persistence length, as well as the hydrodynamical coupling of the fiber with the solvent and the strength of interaction with the substrate *via* surface wetting. The hydrodynamic coupling is described *via* the Einstein–Stokes equation and depends on the diffusion coefficients of the fibers which may change as cytochromes bind the heme, in a manner consistent with the improved imaging of the fibers and the disappearance of the 1H signals in NMR on heme binding. The effect of cytochrome folding on the mechanical properties of the fibers is varied. As shown in Table 4 the addition of heme to BSS results in an apparent increase in the rigidity of the fiber based on

the reduction in angle on adsorption to the substrate. However, Table 4 also shows that the opposite behavior was seen for SSSB where the addition of heme allowed the fiber greater flexibility as it adsorbed to the surface which was evidenced by a decrease in angle. This mechanical behavior has been interpreted according to the position and spacing of the cytochrome within the fiber relative to the underlying helical filaments. Finally, the conformation and spacing of the cytochromes may also affect the ability of the fibers to wet the substrate surface, changing the magnitude and direction of the overall forces on the fiber.

A Generic Model of Amyloid Fiber. The key results of this study have been used to inform the design of the generic coarse grain model depicted in Figure 8 in which a number of identical fundamental units are constrained to a helical space curve and all the units are forcibly oriented to experience identical environments with respect to their nearest neighbors, in a manner consistent with conservation of curvature along the fiber length.

The rationale for this first principle stems from the idea that polymorphism of the protein throughout the amyloid has consequences on the similarity, curvature, and registration of adjacent filaments and is therefore critical in determining the overall long-range morphology of the fiber.

The fundamental unit can, in general, be anything. In this case it comprises a short elliptical rod associated with two spherical domains. Many such units are spaced equidistantly along a helix to form the filament. The ellipsoids within the filament are taken to represent β-strands involved in the helical β-sheet core of the fiber (core material), and the spherical domains are taken to represent arbitrary material that does not contribute to the helical β-sheet backbone of the fiber (noncore material).[26]

It has been shown that short chains of amino acids can generate anisotropy[12] and such anisotropy is sufficient to form helices.[27] Therefore it is physically reasonable to arbitrarily constrain the center of gravity of each unit to a helical space curve. Since there is no difference between the units it is also reasonable to require that, in a minimal energy configuration, the environment for each unit is identical with respect to it is nearest neighbors.

A consequence of these stipulations is that each filament in the construct will have the same curvature and each unit will be in identical registry with other units along the entire fiber. The latter implies the filaments are aligned coaxially, which means the only two remaining degrees of freedom with which to generate the variations in morphology are coaxial longitudinal displacement and a screw displacement for each filament which controls the relative registration,

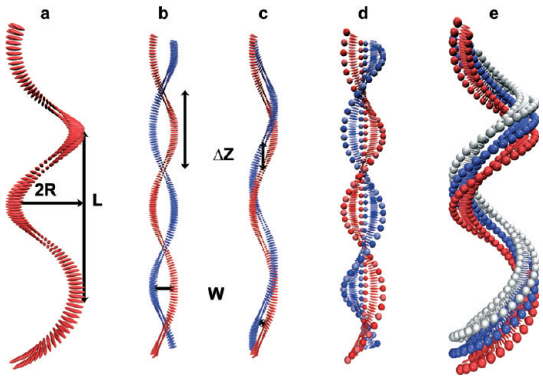

Figure 8. A generic model of fiber structure based on experimental considerations. (a) β-strands, taken to be ~4.8 Å apart, interact anisotropically to form two helicoid β-sheets, ~10 Å apart, in the core of an amyloid filament defined by *L*, denoting pitch length, and *R*, denoting the radius. (b) A twisted ribbon fiber is formed by two filaments maximally displaced along a common axis. (c) Spiral ribbons are formed when the displacement is smaller. The only difference between b and c is the change in displacement of the blue filament measured by ΔZ or *W*. (d,e) The inclusion of proximal and distal spheres emulates the role of noncore material in the fiber.

which will be the same for all the units along the fiber by construction.

It is proposed that these last two degrees of freedom can be mediated by the noncore protein, and this is what gives rise to the variations in morphology encountered in the experimental data, for which the primary difference is the position of the displayed cytochrome within the fusion protein.

These simple first principles result in a model (Figure 8a) that allows continuous variation in morphology from twisted to spiral ribbon (Figure 8b,c) and also for the introduction of excess material that is not contained within the β-sheet core of each filament (Figure 8d,e).

ΔZ and *W* are analytically connected to each other in terms of *L* and *R*[28] because they both arise from the same filament displacement and so in effect are the same parameter.

Figure 8d shows an example of how the noncore material may be introduced into a twisted ribbon and Figure 8e shows a spiral ribbon with noncore material, which also indicates how to generalize to higher numbers of filaments; in this case, three.

A more precise mathematical description of the model, references to other models in the literature, and some discussion of how such a model relates to other experimental evidence is presented elsewhere.[28]

CONCLUSION AND OUTLOOK

The most significant result of this investigation is that the morphology of the adsorbed amyloid fiber can be controllably modified by changes to the noncore

material. This is of immense importance for two reasons:

1. The arrangement of the filaments is intimately mediated by the noncore material.
2. Small molecule control of long-range self-assembled structures is possible.

The generation of a structure, which is mechanically tunable but also has the potential for advanced electronic functionality, represents a step toward emulating the capability of natural systems for controlling quanta at room temperature.

The detailed consideration of the experimental results presented here has led to the definition of a coarse grain model for amyloid which is readily amenable to computation using coarse grain energy minimization,[27] and this is the next logical step to further test the validity of the conclusions against the experimental data.

MATERIALS AND METHODS

Protein Purification. The integrity of all proteins was confirmed by ESI mass spectrometry.

SS, SSB, and SSSB are expressed as GST fusion proteins in *E. coli* strain HMS174 in LB medium. The fusion protein is folded and soluble and is purified on a glutathione column using an AKTA FPLC prior to thrombin cleavage. The cleaved SH3-Cytochrome protein is then purified by anion exchange chromotography on a Mono-Q column with a KCl gradient of 0−200 mM KCl, which separates any naturally occurring holoprotein from apoprotein.

BSSB is produced directly (not as GST fusion protein) and is exported into the *E. coli* periplasm using the natural export signal sequence of cytochrome b562. The protein was expressed in strain NM554, and the periplasm was extracted using standard methods.[29] This extract is acidified to pH 4.6, and insoluble material is removed by centrifugation before adjusting to pH 8.5. The protein is then purified by two rounds of anion exchange chromatography in diethanolamine buffer (20 mM, pH 8.5) using gradients of 0−600 mM KCl, which also separates the apo- and holo-proteins.

BSS is made by proteolytic cleavage of BSSB and purifying again by anion exchange as described above.

Fiber Formation. The formation of SS and SSB fibers is described elsewhere.[6,20] SSSB and BSS fibers are formed in a similar way by incubating the monomers at pH 2 for 5 mins to make them unfold; increasing to pH 3.6 for 15 min makes them partially refold and then reducing to pH 2.2 and incubating at room temperature for seven days allows the fibers to form. The fibers are harvested by ultracentrifugation and resuspension in 1 mM HCl which allows preservation of the fibers at pH 3 while allowing folding of the displayed cytochromes in the presence of heme as proved by NMR.[24]

Low Resolution AFM. Data was collected in air using Veeco Tap150 probes (tip radius < 10 nm, nominal resonant frequency 150 kHz, nominal spring constant 7 N/m) on a Bruker Dimension 3100 with Nanoscope IV controller or a standard Asylum MFP 3D. A 50 μL portion of 10 nM fiber solution was deposited on 1 cm^2 slides of freshly cleaved mica and allowed to adsorb for 1 min prior to blotting with filter paper and subsequent gentle drying in N_2. Images were flattened and processed using standard techniques with the software package SPIP from Image Metrology A/S or WSXM.

High Resolution AFM. Data were collected under liquid in 1 mM HCl on a bespoke low noise AFM using nanosensor SSS-NCH probes (tip radius < 5 nm, 300−350 kHz, < 42 N/m). A 50 μL droplet of 10 nM fiber solution was deposited onto freshly cleaved mica for 20 s, before blotting the sample dry and subsequently introducing the imaging buffer. The images were flattened using Igor Pro. Where possible all measurements are made between topological maxima which limits the effects of tip convolution.

TEM. Images were collected using either a Tecnai 20 or Philips CM100. Approximately 5 μL of 1 μM fibers were deposited on the grid with 5 μL of uranyl acetate stain and allowed to settle. The entire droplet was removed and 5 μL of stain was added again to the droplet before blotting and then drying in air for 10 min. In this way the fibers are negatively stained and appear suspended over the holes in the holey carbon grid. The images were bandpass filtered to remove variations in stain thickness, film thickness, and high frequency information. They were also contrast enhanced prior to measuring the fiber dimensions using the profiling tools available in ImageJ (rsweb.nih.gov/ij/).

Heme Titrations. The fusion proteins all contain tryptophan, which allows reasonable estimation of their extinction coefficients. The total protein concentration of mature fibers solution was found by correcting the UV−vis spectra of apo-fibers for high frequency Mie scattering. The concentration of a filtered stock solution of heme in 1 mM NaOH was determined by adding a small, known volume of the heme solution to a solution containing ~3-fold excess of wild type apocytochrome monomers in 100 mM Tris-HCl buffered at pH 8. This procedure allows the assumption that all the heme is rapidly bound. The extinction coefficient of heme bound in cytochrome b_{562} at pH 8 is well characterized,[30] allowing determination of the concentration of the initial free heme stock. The extinction coefficients of free heme can then be measured at pH 3. Heme can then be added to fibers in varying ratios and allowed to equilibrate for 20 min prior to scanning.

Job Plot. The well characterized free and bound heme extinction coefficients at pH 3 allows the resulting series of spectra to be deconvolved by a nonlinear fitting route or SVD into free and bound heme contributions. This measures the effect of the aggregation state of the protein on the partitioning of the heme population. The proportion of bound heme and free heme can be plotted against the total heme and normalized against the quantity of protein. This results in a Job plot in which the position of the maxima of the curve pertaining to bound heme reveals the stoichiometric ratio of bound heme to protein in the fiber sample.

Conflict of Interest: The authors declare no competing financial interest.

Supporting Information Available: Additional AFM data used in the statistical analysis, extinction coefficients of free and bound heme at pH 3 and pH 8, and a graphical illustration of the techniques used to measure the fibers. This material is available free of charge *via* the Internet at http://pubs.acs.org.

Acknowledgment. C. Forman acknowledges the receipt of a CASE studentship from the UK EPSRC and QinetiQ. This work was also supported by the BBSRC (Grant BB/D019109 to P. Barker) and the Royal Society and the Royal Academy of Ireland (International Travel Grant to P. Barker and S. Jarvis).

REFERENCES AND NOTES

1. Milne, J.L.S.; Shi, D.; Rosenthal, P.B.; Sunshine, J.S.; Domingo, G.J.; Wu, X.W.; Brooks, B.R.; Perham, R.N.; Henderson, R.; Subramaniam, S. Molecular Architecture and Mechanism of an Icosahedral Pyruvate Dehydrogenase Complex: A Multifunctional Catalytic Machine. *EMBO J.* **2002**, *21*, 5587–5598.
2. Yeates, T. O.; Thompson, M. C.; Bobik, T. A. The Protein Shells of Bacterial Microcompartment Organelles. *Curr. Opin. Struct. Biol.* **2011**, *21*, 223–231.

3. Parsons, J. B.; Frank, S.; Bhella, D.; Liang, M.; Prentice, M. B.; Mulvihill, D. P.; Warren, M. J. Synthesis of Empty Bacterial Microcompartments, Directed Organelle Protein Incorporation, and Evidence of Filament-Associated Organelle Movement. *Mol. Cell* **2010**, *38*, 305–315.
4. Efremov, R. G.; Baradaran, R.; Sazanov, L. A. The Architecture of Respiratory Complex I. *Nature* **2010**, *465*, 441–445.
5. Noy, D. Natural Photosystems From an Engineer's Perspective: Length, Time, and Energy Scales of Charge and Energy Transfer. *Photosynth. Res.* **2008**, *95*, 23–35.
6. Baldwin, A. J.; Bader, R.; Christodoulou, J.; MacPhee, C. E.; Dobson, C. M.; Barker, P. D. Cytochrome Display on Amyloid Fibrils. *J. Am. Chem. Soc.* **2006**, *128*, 2162–2163.
7. Page, C. C.; Moser, C. C.; Chen, X.; Dutton, P. L. Natural Engineering Principles of Electron Tunnelling in Biological Oxidation−Reduction. *Nature* **1999**, *402*, 47–52.
8. Jiménez, J. L.; Guijarro, J. I.; Orlova, E.; Zurdo, J.; Dobson, C. M.; Sunde, M.; Saibil, H. R. Cryo-electron Microscopy Structure of an SH3 Amyloid Fibril and Model of the Molecular Packing. *EMBO J.* **1999**, *18*, 815–821.
9. Fukuma, T.; Mostaert, A. S.; Serpell, L. C.; Jarvis, S. P. Revealing Molecular-Level Surface Structure of Amyloid Fibrils in Liquid by Means of Frequency Modulation Atomic Force Microscopy. *Nanotechnology* **2008**, *19*, 384010.
10. Bayro, M. J.; Maly, T.; Birkett, N. R.; Macphee, C. E.; Dobson, C. M.; Griffin, R. G. High-Resolution MAS NMR Analysis of PI3-SH3 Amyloid Fibrils: Backbone Conformation and Implications for Protofilament Assembly and Structure. *Biochemistry* **2010**, *49*, 7474–7484.
11. Ghafouri, R.; Bruinsma, R. Helicoid to Spiral Ribbon Transition. *Phys. Rev. Lett.* **2005**, *94*, 138101.
12. Bellesia, G.; Fedorov, M. V.; Timoshenko, E. G. Structural Transitions in Model Beta-Sheet Tapes. *J. Chem. Phys.* **2008**, *128*, 195105.
13. Sunde, M.; Serpell, L. C.; Bartlam, M.; Fraser, P. E.; Pepys, M. B.; Blake, C. C. Common Core Structure of Amyloid Fibrils by Synchrotron X-ray Diffraction. *J. Mol. Biol.* **1997**, *273*, 729–739.
14. Shiraham, T.; Cohen, A. S. High Resolution Electron Microscopic Analysis of Amyloid Fibril. *J. Cell Biol.* **1967**, *33*, 679–708.
15. Makin, O. S.; Serpell, L. C. Structures for Amyloid Fibrils. *FEBS J.* **2005**, *272*, 5950–5961.
16. Jaroniec, C. P.; MacPhee, C. E.; Bajaj, V. S.; McMahon, M. T.; Dobson, C. M.; Griffin, R. G. High-Resolution Molecular Structure of a Peptide in an Amyloid Fibril Determined by Magic Angle Spinning NMR Spectroscopy. *Proc. Natl. Acad. Sci. U.S.A.* **2004**, *101*, 711–716.
17. Adamcik, J.; Jung, J.-M.; Flakowski, J.; De Los Rios, P.; Dietler, G.; Mezzenga, R. Understanding Amyloid Aggregation by Statistical Analysis of Atomic Force Microscopy Images. *Nat. Nanotechnol.* **2010**, *5*, 4–9.
18. van Gestel, J.; de Leeuw, S. W. The Formation of Fibrils by Intertwining of Filaments: Model and Application to Amyloid Abeta Protein. *Biophys. J.* **2007**, *92*, 1157–1163.
19. Pedersen, J. S.; Andersen, C. B.; Otzen, D. E. Amyloid Structure—One but Not the Same: The Many Levels of Fibrillar Polymorphism. *FEBS J.* **2010**, *277*, 4591–4601.
20. Bader, R.; Bamford, R.; Zurdo, J.; Luisi, B. F.; Dobson, C. M. Probing the Mechanism of Amyloidogenesis through a Tandem Repeat of the PI3-SH3 Domain Suggests a Generic Model for Protein Aggregation and Fibril Formation. *J. Mol. Biol.* **2006**, *356*, 189–208.
21. Smith, B.; Zastavker, Y.; Benedek, G. Tension-Induced Straightening Transition of Self-Assembled Helical Ribbons. *Phys. Rev. Lett.* **2001**, *87*, 26–29.
22. Krebs, M. R. H.; Devlin, G. L.; Donald, A. M. Amyloid Fibril-like Structure Underlies the Aggregate Structure across the pH Range for beta-Lactoglobulin. *Biophys. J.* **2009**, *96*, 5013–5019.
23. Baldwin, A. J.; Anthony-Cahill, S. J.; Knowles, T. P. J; Lippens, G.; Christodoulou, J.; Barker, P. D.; Dobson, C. M. Measurement of Amyloid Fibril Length Distributions by Inclusion of Rotational Motion in Solution NMR Diffusion Measurements. *Angew. Chem., Int. Ed.* **2008**, *47*, 3385–3387.
24. Baldwin, A. J. Solution-State N. M. R. Studies of Amyloid Fibrils. Ph.D. Thesis, University of Cambridge, 2007.
25. Botev, Z. I.; Kroese, D. P.; Grotowski, J. F. Kernel Density Estimation *via* Diffusion. *Ann. Stat.* **2010**, *38*, 2916–2957.
26. This model is generic and makes no claims about the number or structure of β-sheets contributed by the amyloid fiber-forming core sequence in the fusion proteins described here. In particular, it is clear from our observations and this model that the size of the monomeric fiber forming unit determines how large a noncore protein domain can be accommodated in an assembled fiber.
27. Fejer, S. N.; Wales, D. J. Helix Self-Assembly from Anisotropic Molecules. *Phys. Rev. Lett.* **2007**, *99*, 86106.
28. Forman, C. J. Towards the Control of the Morphology of Amyloid Fibrils Displaying Electron Transfer Proteins. Ph.D. Thesis, University Of Cambridge, 2010
29. Barker, P. D.; Nerou, E. P.; Freund, S. M.; Fearnley, I. M. Conversion of Cytochrome b_{562} to c-type Cytochromes. *Biochemistry* **1995**, *34*, 15191–151203.
30. Barker, P. D.; Nerou, E. P.; Cheesman, M. R.; Thomson, a. J.; de Oliveira, P.; Hill, H. a. Bis-methionine Ligation to Heme Iron in Mutants of Cytochrome b_{562}. 1. Spectroscopic and Electrochemical Characterization of the Electronic Properties. *Biochemistry* **1996**, *35*, 13618–13626.